The Mutual Orbit, Mass, and Density of Transneptunian Binary G!kúnǁ'hòmdímà (229762 2007 UK_{126})

W.M. Grundy[1], K.S. Noll[2], M.W. Buie[3], S.D. Benecchi[4], D. Ragozzine[5], and H.G. Roe[6]

1. Lowell Observatory, Flagstaff Arizona.
2. NASA Goddard Space Flight Center, Greenbelt Maryland.
3. Southwest Research Institute, Boulder Colorado.
4. Planetary Science Institute, Tucson Arizona.
5. Brigham Young University, Provo Utah.
6. Gemini Observatory/AURA, Santiago Chile.

— In press in *Icarus* DOI:10.1016/j.icarus.2018.12.037 —

Abstract

We present high spatial resolution images of the binary transneptunian object G!kúnǁ'hòmdímà (229762 2007 UK_{126}) obtained with the Hubble Space Telescope and with the Keck observatory on Mauna Kea to determine the orbit of G!ò'é !hú, the much smaller and redder satellite. G!ò'é !hú orbits in a prograde sense, on a circular or near-circular orbit with a period of 11.3 days and a semimajor axis of 6000 km. Tidal evolution is expected to be slow, so it is likely that the system formed already in a low-eccentricity configuration, and possibly also with the orbit plane of the satellite in or close to the plane of G!kúnǁ'hòmdímà's equator. From the orbital parameters we can compute the system mass to be 1.4×10^{20} kg. Combined with estimates of the size of G!kúnǁ'hòmdímà from thermal observations and stellar occultations, we can estimate the bulk density as about 1 g cm^{-3}. This low density is indicative of an ice-rich composition, unless there is substantial internal porosity. We consider the hypothesis that the composition is not unusually ice-rich compared with larger TNOs and comet nuclei, and instead the porosity is high, suggesting that mid-sized objects in the 400 to 1000 km diameter range mark the transition between small, porous objects and larger objects that have collapsed their internal void space as a result of their much higher internal pressures and temperatures.

Introduction

G!kún‖'hòmdímà[1] (229762 2007 UK_{126}) was discovered by the Palomar Distant Solar System Survey team at a distance of about 46 AU from the Sun (Schwamb et al. 2008, 2009, 2010). It is relatively bright for a transneptunian object (TNO), with an intrinsic visual brightness of 3.7 mag (Perna et al. 2010), in the same league as well-known objects like Varda, Ixion, and Varuna. Its heliocentric orbit has a period of 620 years and a semimajor axis of 74 AU, inclined 21° to the plane of the solar system (averaged over a 10 Myr integration). The mean orbital eccentricity of 0.496 takes it out to aphelion at 110 AU and in to perihelion at 37 AU. Since this perihelion distance is well outside of Neptune's orbit, and the orbit is not in a mean motion resonance with Neptune, G!kún‖'hòmdímà can be classified as a detached object (e.g., Gladman et al. 2008). The Deep Ecliptic Survey (e.g., Elliot et al. 2005) classifies it as a scattered disk object.

Noll et al. (2009) discovered G!ò'é !hú, the much fainter satellite of G!kún‖'hòmdímà, in Hubble Space Telescope images obtained in late 2008. They reported G!ò'é !hú as being 3.8 magnitudes fainter than G!kún‖'hòmdímà, corresponding to nearly a factor of six between the diameters of the two bodies, if both had the same albedo. The existence of a satellite opens the door to a variety of deeper investigations, some of which are described in this paper. Most large TNOs have been found to host satellites, so the existence of a companion for G!kún‖'hòmdímà is not unusual (e.g., Brown et al. 2006; Noll et al. 2008; Parker et al. 2016; Kiss et al. 2017).

Photometric monitoring of the G!kún‖'hòmdímà system revealed a very low amplitude lightcurve, presumed to be due to the rotation of the primary body. Thirouin et al. (2014) reported photometric variation of approximately 0.03 mag peak-to-peak with a best fit rotational period of 11.05 hours, although longer periods of 14.30 and 20.25 hours were also considered possible. Folding in the ambiguity between single-peaked lightcurves caused by albedo patterns and double-peaked lightcurves caused by elongated shapes, it is probably safe to say that the rotation period is at least 11 hours, but not longer than 41 hours.

Santos-Sanz et al. (2012) used Herschel PACS thermal infrared observations of G!kún‖'hòmdímà at 70, 100, and 160 μm wavelength to estimate the surface area of the system as equivalent to a sphere of diameter 599 ± 77 km. Benedetti-Rossi et al. (2016) reported successful observations from seven stations of a stellar occultation by G!kún‖'hòmdímà on 2014 Nov. 15, tracing a limb with an elliptical profile. They processed the data in two different ways, resulting in a pair of solutions with the position angle of the short axis of the ellipse at 129^{+14}_{-22} or

1 The names are proposed to the International Astronomical Union's Small Bodies Nomenclature Committee. G!kún‖'hòmdímà is the beautiful aardvark girl of Ju|'hoan mythology who sometimes appears in stories as a python and sometimes as an elephant. She defends her people and punishes wrongdoers using g‖ámíg‖àmì spines, a raincloud full of hail, and her magical oryx horn, g!ò'é !hú (Biesele 1993, 2009). The Ju|'hoan orthography symbols !, |, and ‖ represent postaveolar, dental, and lateral clicks, while diacritic marks ´ and ` on vowels indicate high and low tones (Dickens 1994). Audio recordings are available at http://www2.lowell.edu/~grundy/tnbs/229762_how_to_say.html.

134^{+14}_{-17} degrees east of north, corresponding to equivalent diameters for G!kún‖'hòmdímà of 638^{+28}_{-14} and 638^{+24}_{-12} km, respectively. Schindler et al. (2017) analyzed two of the seven Benedetti-Rossi et al. chords, plus one additional, high signal-to-noise, near-central chord. They incorporated constraints from the Herschel space telescope thermal observations by arguing that the spectral energy distribution favored a low sub-solar latitude, within ±45° of the equator. Their solution for the elliptical shape of G!kún‖'hòmdímà's shadow had its short axis at a position angle of 158.75 ± 5.65 east of north, which they interpreted as the projection of a Maclaurin spheroid with *a*/*c* axis ratio between 1.08 and 1.22, with a volume corresponding to that of a sphere with diameter 599 to 629 km. Both groups combined their sizes with ground-based photometry to constrain the visual wavelength albedo of G!kún‖'hòmdímà, obtaining $0.159^{+0.007}_{-0.013}$ (Benedetti-Rossi et al. 2016) and 0.150 ± 0.016 (Schindler et al. 2017). These albedos can be compared to those of comparably-sized transneptunian bodies. Varda has a very similar albedo at $0.166^{+0.043}_{-0.033}$ (Grundy et al. 2015), while Salacia (0.042 ± 0.004), 55637 (0.10 ± 0.01), and Quaoar (0.12 ± 0.01) have lower albedos and Orcus (0.23 ± 0.02) is brighter still (Brown and Butler 2017).

These mid-sized TNOs between around 400 and 1000 km in diameter are especially interesting in occupying a transition region between smaller TNOs that generally have low bulk densities, and planet-sized bodies like Pluto, Eris, and Haumea with higher densities. By exploring this transition region, it may be possible to learn whether the transition is due to large and small bodies having formed in distinct nebular regions from different initial compositions (e.g., Brown 2013). Alternatively, the transition could mark where objects reached high enough internal pressures and temperatures to begin to collapse their internal pore space or even trigger internal melting and differentiation.

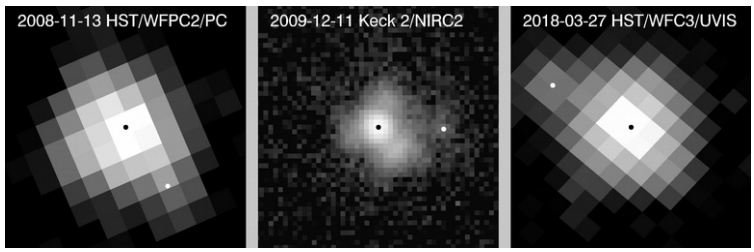

Fig. 1. Example frames from the 3 different telescope/instrument combinations we used to observe G!kún‖'hòmdímà, logarithmically stretched to reveal the much-fainter G!ò'é !hú. Black and white dots mark best fit locations of G!kún‖'hòmdímà and G!ò'é !hú, respectively, from the ensemble of frames associated with each visit. Each panel is ½ arcsec on a side, with North up and East to the left. The spatial sampling of Keck NIRC2 is clearly superior, although the PSF exhibits a complicated and time-variable trefoil pattern in the Airy ring.

Data sources and processing

We obtained observations that spatially resolve G!ò'é !hú from G!kún‖'hòmdímà from three instruments at two telescopes: WFPC2/PC and WFC3/UVIS at the 2.4 m Hubble Space Telescope (HST) and NIRC2 at the 10 m Keck 2 telescope on the summit of Mauna Kea in Hawai'i. Example images are shown in Fig. 1, illustrating the distinct characteristics of

the three instruments.

G!ò'é !hú was first detected in 2008 using HST's WFPC2/PC camera (McMaster et al. 2008; Dolphin 2009), with observations obtained as part of HST program 11113 (Noll et al. 2009). An example frame is shown in the left panel of Fig. 1. The discovery observation consisted of four frames dithered in a box pattern to help overcome the instrument's coarse sampling of the telescope's pointspread function (PSF) with its 0.046 arcsec pixels. Each exposure was 260 sec using the *F606W* filter with pivot wavelength 0.6001 μm and RMS bandwidth 0.0638 μm. We fitted a pair of Tiny Tim model PSFs (Krist et al. 2011) to each image to obtain the locations of the two bodies, holding the focus fixed. For three of the four frames, the relative locations were consistent, but for the 1st frame of the visit, we obtained inconsistent results possibly due to cosmic ray contamination, so that one was excluded from the mean. Mean values are in Table 1, along with uncertainties estimated from the scatter of the three good frames. Additional details of our procedures for processing WFPC2/PC images of binary TNOs can be found in Grundy et al. (2009).

Table 1
Observation circumstances and relative astrometry

UT date and time	Telescope/ instrument	r (AU)	Δ (AU)	g (deg.)	Δx (arcsec)	Δy (arcsec)	Δmag (mag)
2008/11/13 $6^h.6453$	HST/WFPC2	45.566	44.658	0.50	−0.0871(37)	−0.1215(28)	3.66(17)
2009/12/11 $8^h.1909$	Keck/NIRC2	45.179	44.334	0.65	−0.1355(60)	−0.0039(60)	3.088(90)
2009/12/12 $7^h.8693$	Keck/NIRC2	45.178	44.339	0.66	−0.1802(60)	−0.0681(60)	3.12(10)
2018/01/02 $14^h.8158$	HST/WFC3 UVIS	42.450	41.674	0.82	−0.1357(35)	−0.1340(14)	3.168(85)
2018/01/03 $11^h.2558$	HST/WFC3 UVIS	42.449	41.680	0.83	−0.0832(39)	−0.1357(10)	3.297(77)
2018/03/27 $7^h.6054$	HST/WFC3 UVIS	42.378	42.797	1.22	+0.1628(26)	+0.0866(10)	3.389(48)
2018/03/31 $6^h.7471$	HST/WFC3 UVIS	42.375	42.850	1.18	−0.060(60)	−0.005(60)	-
2018/08/04 $23^h.0537$	HST/WFC3 UVIS	42.267	42.732	1.22	−0.1617(10)	−0.1061(15)	3.212(26)

Table notes:

[a.] The distance from the Sun to the target is r and from the observer to the target is Δ. The phase angle g is the angular separation between the observer and Sun as seen from the target.

[b.] Relative right ascension Δx and relative declination Δy are computed as $\Delta x = (\alpha_2 - \alpha_1)\cos(\delta_1)$ and $\Delta y = \delta_2 - \delta_1$, where α is right ascension, δ is declination, and subscripts 1 and 2 refer to G!kún‖'hòmdímà and G!ò'é !hú, respectively. Estimated 1-σ uncertainties in the final 2 digits are indicated in parentheses.

[c.] The mean magnitude difference Δmag between primary and secondary for each visit is shown in the last column with 1-σ uncertainties in the final 2 digits indicated in parentheses. No Δmag was computed for the 2018 March 31 visit because the sources were so highly blended.

[d.] A machine readable version of this table is provided as supplementary on-line material.

We next observed the system on two consecutive nights in December 2009 using adaptive optics (AO) at the Keck 2 telescope, our first use of that system to observe binary TNOs. These objects are much too faint to use for wavefront sensing, so our observation used the artificial laser guide star AO (LGS AO) mode (Le Mignant et al. 2006). The laser creates a bright point-like source in the upper atmosphere suitable for measuring atmospheric distortion of the incoming wavefront, but in addition to the laser, a nearby moderately bright source is required for low-order tip-tilt correction. G!kúñ'hòmdímà is too faint even for that, so our observations exploited a stellar appulse. The motion of G!kúñ'hòmdímà relative to the appulse star was handled using differential tracking software developed by A. Conrad. The observations were done in the near-infrared *H* filter, with central wavelength 1.633 μm and bandpass width 0.296 μm. Exposure times were 60 sec on the first night and 90 sec on the second night. To minimize the overhead cost of dithering, we took 3 consecutive images in one pointing, before offsetting the telescope and collecting 3 more, etc. The 9.95×10^{-3} arcsec pixels of NIRC2's narrow-field camera do an excellent job of sampling the PSF, so the point of dithering was to overcome the relatively sparse bad pixels. We collected 3 sets of 3 images the first night, and attempted to do the same the second night, but the 2nd offset did not work, so we ended up with 3 frames in the first pointing and 6 more in the second. We coadded all of the images in each pointing, masked any lobe of the primary's Airy ring that fell near the location of the secondary, and then fitted circularly symmetric Lorentzian PSFs to the central cores of the two sources, using the Amoeba downhill simplex minimization scheme (Nelder and Mead 1965; Press et al. 1992) to iteratively adjust the locations, brightnesses, and shared full width at half maximum of the two PSFs to minimize the χ^2 statistic between data and model images. The quality of the AO correction was time-variable, and we were not able to see G!ò'é !hú in the second of the three coadded stacks from the first night, so from each night we ended up with just two sets of measurements which were averaged together to obtain the nightly mean astrometry shown in Table 1. With so few positions informing each average, we did not obtain a good measure of the astrometric uncertainty. We crudely estimate it as ±0.006 arcsec, based on subsequent experience with the instrument (e.g., Grundy et al. 2011, 2015). This uncertainty is consistent with the difference between the observed and predicted locations in our final orbit fit.

A final set of observations was done in 2018 using HST's WFC3/UVIS camera (e.g., Bellini et al. 2011; Dressel 2018) through program 15233, which consisted of five single HST-orbit "visits" to the G!kúñ'hòmdímà system. Each visit consisted of 4 box-dithered 192 sec exposures using the *F606W* filter (WFC3's *F606W* filter is slightly different from WFPC2's, with pivot wavelength 0.5885 μm and RMS bandwidth 0.0657 μm). This pattern of 4 exposures was split in half, with another set of 4 box-dithered 392 sec exposures in a different filter, either *F814W* or *F438W*, sandwiched into the middle. These two filters have pivot wavelengths of 0.8044 and 0.4325 μm and RMS bandwidths of 0.0670 and 0.0197 μm, respectively. The purpose of book-ending the other filter observations with *F606W* observations was to minimize potential lightcurve effects on the retrieved colors. A pair of model Tiny Tim PSFs was fitted to each image, using the model focus for the time of each frame from http://focustool.stsci.edu/cgi-bin/control.py. The average relative astrometry for each visit is reported in Table 1. More details

on our processing of WFC3 images can be found in Grundy et al. (2014; 2015). G!ò'é !hú was too close to G!kúnǁ'hòmdímà to be well resolved in the 4th visit (March 31 UT) resulting in much larger astrometric uncertainty, but for the remaining visits, the scatter in astrometric measurements of individual frames indicated uncertainties in the 0.001 to 0.004 arcsec range.

Table 2
WFC3 UVIS Photometry

UT Date	G!kúnǁ'hòmdímà brightness (mag)				G!ò'é !hú brightness (mag)			
	F606W	***V***	***F814W***	***I***	***F606W***	***V***	***F814W***	***I***
Jan. 2	19.528(23)	19.761(23)	18.646(30)	18.653(30)	23.034(77)	23.492(77)	21.756(92)	21.796(92)
Jan. 3	19.660(58)	19.893(58)	18.954(32)	18.961(32)	23.327(34)	23.785(34)	21.65(16)	21.69(16)
Mar. 27	19.6085(85)	19.8415(85)	18.817(22)	18.824(22)	23.324(63)	23.783(63)	21.885(97)	21.926(97)
Aug. 4	19.607(19)	19.840(19)	18.836(41)	18.843(41)	23.13(12)	23.58(12)	21.867(43)	21.908(43)

Table note:
[a.] A machine readable version of this table is provided as supplementary on-line material.

The weighted mean of the relative photometry is $\Delta_{mag} = 3.242 \pm 0.039$ mag, somewhat smaller than the 3.8 mag value we had reported on discovery of G!ò'é !hú (Noll et al. 2009). This value corresponds to a factor of 4.45 ± 0.08 difference in radius, assuming G!kúnǁ'hòmdímà and G!ò'é !hú share the same albedo, which may not be the case. It is also important to recognize that this average combines data obtained at various different wavelengths.

Visit mean WFC3 photometric measurements in *F606W* and *F814W* filters are listed in Table 2. These values correspond to Johnson *V-I* colors for G!kúnǁ'hòmdímà and G!ò'é !hú of 1.028 ± 0.027 and 1.803 ± 0.084, respectively, or linear color slopes of 13.23 ± 0.97 and 68.2 ± 2.9, defined as percent spectral rise per 100 nm wavelength, normalized at *V* (e.g., Hainaut and Delsanti et al. 2002). At these wavelengths, the two bodies are distinctly different in color, with G!ò'é !hú being significantly redder than G!kúnǁ'hòmdímà. This dichotomy contrasts with the similarity of primary and secondary colors reported for more equal-sized binaries (Benecchi et et. 2009). However, among the larger, planet-sized TNOs, small satellites do tend to differ in color from their primary bodies (e.g., Carry et al. 2011), so this color contrast is not anomalous. What is perhaps more of a surprise is just how extremely red G!ò'é !hú appears to be. Its *V-I* color is among the reddest reported for any TNO.

Orbit determination

As soon as we obtain astrometric data on a binary TNO, we begin searching for possible Keplerian mutual orbits using Monte Carlo techniques described by Grundy et al. (2008). This sampling produces collections of orbits consistent with the available data. Initially, the available data do not uniquely determine the orbit so a broad swath of orbital element space is populated, but each subsequent astrometric measurement whittles away at the allowed region of orbital element space, eventually splitting it into discrete clumps, and ultimately excluding all but one of

those clumps. The last such solution clumps to be eliminated involved orbital periods of 5.80, 6.70, 7.18, 8.61, 12.73, 15.39, and 17.94 days. All had χ^2 above 100 enabling them to be confidently excluded, thanks to the strategic timing of the last few observations. This process of elimination is aided by the fact that the system is observed from directions that change slowly over the course of time due to the motions of Earth and G!kún‖'hòmdímà around the Sun. With observations spanning about a decade, sufficient parallax has accumulated to confidently exclude the orbit solution that is the mirror image through the sky plane of the actual orbit. This parallax is illustrated in Fig. 2. After the space of allowed orbits has collapsed to a clump, we use the downhill simplex algorithm to iteratively adjust the Keplerian orbital elements to minimize the χ^2 statistic between observed astrometry and model positions to find the best fit Keplerian orbit solution for that clump. For a viable solution, we assess the uncertainties in these elements by randomizing the observed astrometric measurements consistent with their observational uncertainties and re-doing the fit, repeating the process 1000 times to get a collection of 1000 solutions that provide a probability distribution around the best fit orbit. Our best fit orbit solution and associated uncertainties are in Table 3.

A Maclaurin spheroid with axis ratio of 1.2 would lead to a precession period due to J_2 of roughly 100 years. Though we have observed an appreciable fraction of this period, we do not have sufficient data to fully justify the inclusion of three additional parameters (J_2 and the spin axis direction) to our fit, especially as we only have three (weaker) observations in the earlier 2008-2009 epoch. We believe that the choice of a Keplerian model does not introduce significant systematic uncertainties into our solution or subsequent interpretation.

Mass and Density

From the mutual orbit, we can compute the total mass of the system, M_{sys}, as

$$M_{sys} = \frac{4\pi^2 a^3}{P^2 G} \quad , \qquad \text{(Eq. 1)}$$

where a and P are the mutual orbit semimajor axis and period, and G is the gravitational constant, taken to be 6.67428×10^{-11} m^3 kg^{-1} s^{-2} (Mohr et al. 2008). We find a system mass of $(1.361 \pm 0.033) \times 10^{20}$ kg. This mass is slightly greater than the system mass of transneptunian binary 55637 (2002 UX$_{25}$) at $(1.25 \pm 0.03) \times 10^{20}$ (Brown 2013) and about half the mass of Varda and Ilmarë $(2.664 \pm 0.064) \times 10^{20}$ kg (Grundy et al. 2015). These objects are all in the mid-size regime of 400 to 1000 km diameter TNOs. It is especially interesting to compute their densities, since these objects appear to be transitional between smaller, low density objects and larger planet-sized bodies with higher densities.

The mean density is computed by dividing the system mass by an estimate of the sum of the volumes of the two component bodies. Considering the various size ranges reported in the literature (e.g., Benedetti-Rossi et al. 2016; Schindler et al. 2017) we adopt an effective diameter for G!kún‖'hòmdímà of 632 ± 34 km, corresponding to a sphere with the volume of G!kún‖'hòmdímà. If G!ò'é !hú has the same albedo and shape as G!kún‖'hòmdímà, its effective diameter is a factor of 4.45 ± 0.08 smaller, or 142 ± 8 km, and we arrive at a total volume of

Table 3
Orbit solution and 1-σ uncertainties

Parameters and units		Values
Fitted elements[a]		
Period (days)	P	11.31473 ± 0.00016
Semimajor axis (km)	a	6035 ± 48
Eccentricity	e	0.0236 ± 0.0066
Inclination[b] (deg)	i	43.75 ± 0.38
Mean longitude[b] at epoch[c] (deg)	ϵ	344.0 ± 1.4
Longitude of ascending node[b] (deg)	Ω	110.6 ± 1.5
Longitude of periapsis[b] (deg)	ϖ	91 ± 18
Derived parameters		
Standard gravitational parameter GM_{sys} (km^3 s^{-2})	μ	9.08 ± 0.22
System mass[d] (10^{18} kg)	M_{sys}	136.1 ± 3.3
Orbit pole right ascension[b] (deg)	α_{pole}	20.6 ± 1.5
Orbit pole declination[b] (deg)	δ_{pole}	46.25 ± 0.32
Orbit pole ecliptic longitude[e] (deg)	λ_{pole}	38.3 ± 1.0
Orbit pole ecliptic latitude[e] (deg)	β_{pole}	34.47 ± 0.63
Inclination between mutual and heliocentric orbits (deg)		32.28 ± 0.64
Next mutual events season (year)		2050

Table notes:

[a.] Elements are for the motion of G!ò'é !hú relative to G!kún‖'hòmdímà. For the full solution χ^2 is 11.3, based on observations at 8 epochs. The mirror orbit solution has a much worse $\chi^2 = 54$, allowing us to exclude it with greater than 5-σ confidence. The best fit circular solution has $\chi^2 = 26.5$, allowing it to be excluded with almost 3-σ confidence.

[b.] Referenced to J2000 equatorial frame.

[c.] The epoch is Julian date 2457000, corresponding to 2014 December 8 12:00 UT.

[d.] Based on the CODATA 2006 value of the gravitational constant $G = 6.67428 \times 10^{-11}$ m^3 s^{-2} kg^{-1} (Mohr et al. 2008).

[e.] Referenced to J2000 ecliptic frame.

$(1.35 \pm 0.22) \times 10^8$ km^3, leading to an average bulk density $\rho = 1.04 \pm 0.17$ g cm^{-3}. If G!ò'é !hú has a lower albedo, similar to the reported albedo contrast between satellites and primaries of larger TNOs by Brown and Butler (2017), then the average bulk density of the system would be

smaller, but Schindler et al. (2017) argued from the thermal data that G!ò'é !hú is unlikely to have a low albedo. If it has a higher albedo than G!kún‖'hòmdímà, then its size would be smaller, and the total volume lower, leading to a higher bulk density. However, under our assumption of equal albedos, G!ò'é !hú only accounts for about 1% of the total volume, so changing its assumed albedo or allowing it to have a different density from G!kún‖'hòmdímà can only perturb the system average density by a modest fraction, much smaller than our reported uncertainty, which is dominated by the uncertainty in the volume of G!kún‖'hòmdímà.

The mean density of G!kún‖'hòmdímà is compared with those of other transneptunian objects in Fig. 3. Objects smaller than about 400 km diameter generally have low densities, indicative of substantial porosity, even if they have very ice rich compositions. Their densities are not unlike those of much smaller comet nuclei, such as 67P/Churyumov-Gerasimenko, at 0.532 ± 0.007 (Jorda et al. 2016). Comet nuclei have substantial non-ice content (e.g., Nagdimunov et al. 2014; Lamy et al. 2015; Fulle et al. 2017, 2019) so their low densities indicate extremely high porosity, consistent with very loosely compacted material. Large objects like Pluto, Triton, Eris, and Haumea have substantially higher densities, also indicative of significant amounts of rock in their interiors in addition to ice, even if they have zero internal porosity.

Brown (2013) pointed to 55637 (2002 UX_{25}) as an especially interesting object, with a low density but a relatively large size (~700 km diameter), arguing that an object that large should not be porous like a small comet nucleus, so it must have a very low rock fraction. An ice-rich composition would be inconsistent both with bulk compositions of comet nuclei and with the compositions of larger planet-sized transneptunian objects like Eris, Pluto, and Haumea, suggesting accretion in a nebular zone endowed with a very different mix of solids or perhaps the result of some other mechanism. This work places another point in the same region of the plot, with G!kún‖'hòmdímà being about the same size as 55637, and having only a slightly higher density.

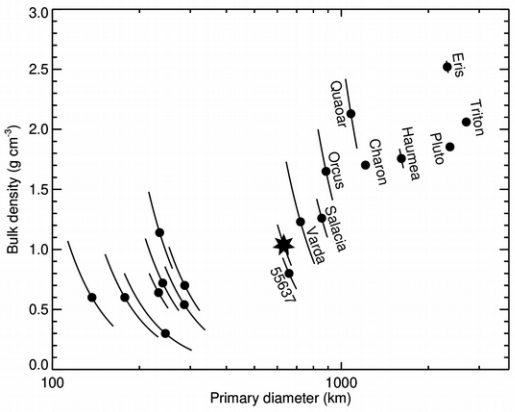

Fig. 3. Densities and sizes of trans-neptunian bodies, with G!kún‖'hòmdímà indicated by a star. Other values are from Benecchi et al. (2010), Brown et al. (2010), Sicardy et al. (2011), Grundy et al. (2012), Stansberry et al (2012), Brown (2013), Fornasier et al. (2013), Vilenius et al. (2012, 2014), Grundy et al. (2015), Brown and Butler (2017), McKinnon et al. (2017), and Ortiz et al. (2017).

Density can provide a valuable constraint on composition, but it does not uniquely determine it. Two issues muddy the water. The first is that rock and water ice are not the only possible ingredients. Additional volatile ices such as CO_2 or CH_4 could exist in these objects, as could carbonaceous material. The convention is to ignore such components and interpret densities only in terms of water ice and rock. Another complicating factor is porosity. Porosity is presumed to be negligible for planet-sized objects, due to their elevated internal pressures and temperatures. But for small

bodies, porosity can be substantial. For Churyumov-Gerasimenko, it in the range of 70 to 75% of the total volume (Jorda et al. 2016). It is not clear what the size threshold should be for TNOs to collapse their pore space. The range of possible porosities and ice/(ice+rock) mass fractions consistent with our density estimate is shown by the curved gray band in Fig. 4. If there is no internal porosity, the composition would have to be nearly pure ice, but even if the composition was pure rock (assumed to have a density of 3 g cm^{-3} here), the porosity would not need to be quite as high as reported for Churyumov-Gerasimenko.

The overburden pressure within a spherical object with a uniform internal mass distribution as a function of the distance from the center of the body *r* is

$$P(r) = \frac{2}{3}\pi\rho^2 R^2 G\left(1-\frac{r^2}{R^2}\right), \qquad \text{(Eq. 2)}$$

where *R* is the radius. For a body with *R* = 316 km and ρ = 1.04 g cm^{-3}, the central pressure *P*(*r*=0) would be 15 MPa. Would such a pressure collapse internal pore space? Durham et al. (2005) performed laboratory piston-cylinder compression studies on pure, granular H_2O ice at 77 K and pressures up to 150 MPa. From initial porosities in the 40% range, they found that even after compaction at 150 MPa pressure, some 10% pore space remained and at 15 MPa, 20 to 25% pore space remained. How these results would change with addition of a significant amount of rock is not known, but it seems likely that rock would increase the resistance to compaction. Omura and Nakamura (2018) extrapolated laboratory experiments with silica sand to show that a 200 km rocky asteroid can maintain ~50% bulk porosity, and indeed porosities this high have been measured for asteroids up to ~300 km diameter, albeit with large uncertainties (Baer et al. 2011). These studies support the idea that rock can maintain significant porosity in bodies approaching the sizes of the mid-size TNOs. Hence, one resolution to the dilemma raised by Brown (2013) is for ice+rock mixtures to maintain similar amounts of porosity as pure rock, allowing for internal properties that are self-consistent and reasonable both geophysically and cosmochemically. Since differentiation would presumably decrease porosity, we assume that ice and rock are intimately mixed, but the same argument could perhaps be extended to a porous rocky core overlaid by an icy mantle.

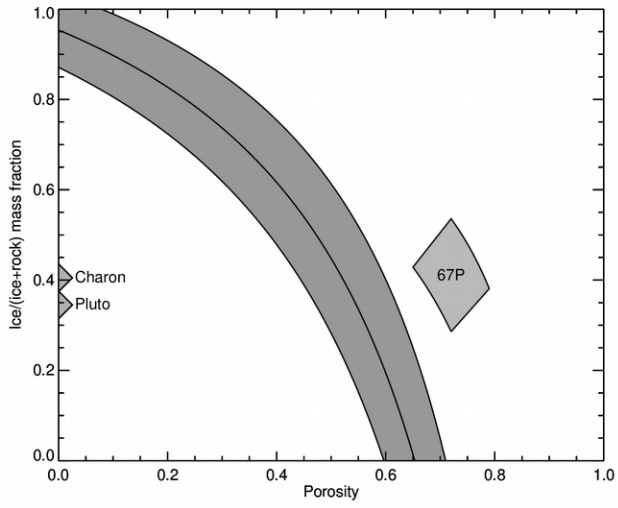

Fig. 4. Interpretation of the density of G!kún‖'hòmdímà in terms of cold H_2O ice (ρ = 0.945 g cm^{-3}), rock (ρ = 3 g cm^{-3}), and void space, compared with ice/(ice+rock) fractions for Pluto and Charon (assuming zero porosity) and for Churyumov-Gerasimenko.

At low temperatures, H_2O ice is brittle and does not flow, but at warmer temperatures, solid-state flow can facilitate the collapse of void space. Rheological behavior of solids is extremely sensitive to

temperature. Thermal models have been used to assess how warm the interiors of various size TNOs could have become (e.g., Merk and Prialnik 2003, 2006; Prialnik et al. 2008; Mckinnon et al. 1997, 2008). If the bodies accreted early enough for short-lived radionuclides ^{26}Al or ^{60}Fe to be incorporated, even relatively small objects could have reached elevated internal temperatures, while if accretion occurred later, longer-lived radionuclides like ^{235}U, ^{238}U, ^{232}Th, and ^{40}K would provide the main sources of radiogenic heat. Another source of heat is from accretion itself, a combination of gravitational potential energy and kinetic energy. The latter depends on the nature of the accretion. For gravitational collapse from locally over-dense regions of the protoplanetary nebular (e.g., Youdin and Goodman 2005; Nesvorný et al. 2010; Simon et al. 2016, 2017), kinetic energy could be a relatively minor factor, but if the late stages of accretion occurred in an environment with a large velocity dispersion, appreciable kinetic energy could be delivered through impacts. Slow accretion allows more time for radiative emission of heat from accretion whereas rapid assembly sequesters more of that heat in the body's interior. Crystallization of initially amorphous ice is another potentially important heat source, but crystallization also expels entrapped volatiles such as CO, which may diminish the heating contribution from crystallization. Such volatiles can provide an efficient mechanism for redistribution of internal heat through latent heat of vaporization. Considering the interplay of all these factors and their sensitivity to the timing and nature of the accretion process, there is considerable uncertainty about the internal thermal history of small and mid-sized TNOs.

We propose that the argument can be turned around by postulating that small and mid-sized TNOs formed with rock-rich compositions comparable to the Pluto system and to Churyumov-Gerasimenko, as argued by Barr and Schwamb (2016). If they have this composition, then the low densities of mid-size TNOs like G!kúnǁ'hòmdímà and 55637 must be telling us that their accretion occurred late enough or slowly enough to maintain low internal temperatures so that they never managed to collapse much of their primordial porosity. Alternatively, the ice+rock mixture may have its strength dominated by rock, such that the thermal properties of the ice are less important. Overburden pressure, impacts, and heat from formation are presumably insufficient to significantly affect the strength of the rock, since temperatures never approach its melting temperature, and we can also call on the empirical observations of large rocky asteroids with high bulk porosities.

Orbital evolution

The likely spin period for G!kúnǁ'hòmdímà of between 11 and 41 hours (Thirouin et al. 2014) is much shorter than the 11.3 day orbital period of G!ò'é !hú, indicating that the system has not tidally synchronized the rotation of G!kúnǁ'hòmdímà to G!ò'é !hú's orbit, as is the case for Pluto and Charon. Following Goldreich and Soter (1966), we can estimate the time scale for that to happen, as

$$\tau_{\mathrm{despin}_1} = \delta\omega_1 \frac{M_1 a^6 Q_1'}{G M_2^2 R_1^3} \quad , \qquad \text{(Eq. 3)}$$

where $\delta\omega_1$ is the change in angular frequency to despin G!kúnǁ'hòmdímà, taken to be the

difference in angular frequency between rotation periods of 11 hours and 11.3 days, or 0.00015 s^{-1}. The masses of G!kúnǁ'hòmdímà and G!ò'é !hú are M_1 and M_2, respectively, a is the semimajor axis of their mutual orbit, and R_1 is the radius of G!kúnǁ'hòmdímà. The specific tidal dissipation factor Q_1 describes the response of G!kúnǁ'hòmdímà to tidal distortion. It is approximately $1/(2\varepsilon)$, where ε is the angle by which the tidal bulge raised by G!ò'é !hú lags behind the sub-G!ò'é !hú longitude. Typical Q values for solid bodies are in the 10 to 100 range (e.g., Goldreich and Soter 1966). Small bodies require a correction from Q to Q', obtained by dividing Q by the Love number k_2 when rigidity is large compared to self-gravity (e.g., Hubbard 1984). This correction works out to $Q' = Q(1+19\mu)/(2g\rho R)$, where μ is the rigidity, g is the surface gravity, and ρ is the density. A lower limit for the rigidity can be taken as 10^6 N m^{-2}, appropriate for a loose sand pile (Yoder 1982). For the fastest possible tidal evolution, we assume $Q = 10$ and $\mu = 10^6$ N m^{-2}, obtaining a lower limit despinning timescale of 2×10^{10} years. Since this timescale is more than the age of the solar system, it is no surprise that G!kúnǁ'hòmdímà is still spinning faster than G!ò'é !hú's orbital period. We can reverse the indices for primary and secondary and estimate a much shorter minimum despinning timescale of G!ò'é !hú as 5×10^7 years. The timescale increases proportionally for larger values of Q and μ. An upper limit for μ can be taken as 4×10^9 N m^{-2}, appropriate for a monolithic block of ice (Gladman et al. 1996). Using this higher value for μ along with $Q = 100$, we obtain an upper limit despinning timescale for G!ò'é !hú of 2×10^{11} years, so whether or not it should be synchronized depends on its rigidity, effective Q, and tidal evolution history (e.g., Hastings et al. 2016). Extremely sensitive long duration lightcurve monitoring, such as has been done using the Kepler spacecraft (e.g., Ryan et al. 2017) might be able to determine the rotation period of G!ò'é !hú in addition to pinning down the rotation of G!kúnǁ'hòmdímà, providing some constraint on its internal structure.

Similarly, following Murray and Dermott (1999), we can estimate the time for the orbit to circularize as

$$\tau_{\text{circ}} = \frac{4}{63}\frac{M_2}{M_1}\frac{a^5}{R_2^5}\frac{Q_2'}{n} \quad , \qquad \text{(Eq. 4)}$$

where n is G!ò'é !hú's mean angular motion. Again using $Q = 10$ and $\mu = 10^6$ N m^{-2}, we estimate a lower limit to the circularization timescale of 10^9 years, and it could be much longer that that, suggesting that the binary may have formed with a low eccentricity, rather than evolving to that state. The best fit eccentricity is small, but not exactly zero at 0.0236 ± 0.0066. Although this eccentricity is more than a factor of three larger than its 1-σ error bar, we would treat that result with caution, since we often find slightly non-zero eccentricities, especially when sampling of orbital longitudes is sparse or uneven, as it is in this case. Eccentricity is a free parameter in our Keplerian orbit fit. If it is not needed to describe the orbit, the minimization routine will use it to compensate for noise in one or more of the astrometric measurements. Our best fit forced-circular orbit solution has $\chi^2 = 26.5$, and can only be rejected at 2.8-σ confidence.

Tidal interaction is a potential source of internal energy, in addition to energy from accretion and the decay of radioactive elements. An upper limit to heating from this source can be estimated by computing the energy required to spin up G!kúnǁ'hòmdímà from non-spining to its

fastest possible spin period of 11 hours and to launch G!ò'é !hú into its present day orbit. The first works out to 3.4×10^{21} J and the second to 1.1×10^{20} J. Dividing the sum of these energies by the mass of G!kún‖'hòmdímà yields a specific energy of 26 J kg^{-1}, insufficient to contribute appreciably to internal heating, considering that the heat capacity of low temperature ice between 40 and 100 K is in the range from 340 to 880 J K^{-1} kg^{-1} (Giauque and Stout 1936).

It is interesting to compare the orientation of G!ò'é !hú's orbit with the orientation of the elliptical limb profile of G!kún‖'hòmdímà seen in the stellar occultation. At the time of the 2014 occultation, our orbit pole would have projected onto the sky plane at a position angle of −34° (or 146° for the anti-pole), which compares with the reported position angles for the short axis of the elliptical limb profile of 129^{+14}_{-22} or 134^{+14}_{-17} degrees (Benedetti-Rossi et al. 2016) and 158.75 ± 5.65 degrees (Schindler et al. 2017). Our anti-pole is consistent with all three orientations to within 3-σ tolerance. However, the same could be said for any orbit pole orientation that projects to the sky plane at a position angle between 142° and 171° or between −9° and −38°. The probability of a random orbit's pole falling within those intervals is about 16%, so although G!kún‖'hòmdímà's spin axis may coincide with G!ò'é !hú's orbit pole, the data are insufficiently constraining to prove such an alignment. The timescale for reorienting G!kún‖'hòmdímà (or, alternatively, for damping the inclination of G!ò'é !hú's orbit relative to G!kún‖'hòmdímà's equator) is roughly similar to the very-long despinning timescale of G!kún‖'hòmdímà. Hence, if they are indeed aligned, they are likely to have formed that way rather than having evolved to that state through subsequent tidal interaction.

Other attributes of G!ò'é !hú's orbit offer potential clues to its origin. The Hill radius of the system at perihelion is computed as

$$r_{\mathrm{H}} = a_{\odot}(1-e_{\odot})\left(\frac{M_{sys}}{3\,M_{\odot}}\right)^{1/3} , \qquad \text{(Eq. 5)}$$

where $a_{\odot}$ and $e_{\odot}$ are the semimajor axis and eccentricity of the heliocentric orbit, and $M_{\odot}$ is the mass of the Sun. The mean separation of the mutual orbit a = 6035 ± 48 km is about 0.38% of the 1.6×10^6 km Hill radius. This measure makes it among the more tightly bound of trans-neptunian binaries with known orbits. Other systems that are comparably tightly bound include Salacia-Actaea, Orcus-Vanth, Varda-Ilmarë, and 55637. These systems also stand out in having low values for the specific orbital angular momentum, the ratio of the angular momentum of the satellite orbit to $\sqrt{G M_{\mathrm{sys}}^3 R_{\mathrm{eff}}}$, where R_{eff} is the radius of a sphere combining the volume of both bodies. For G!kún‖'hòmdímà, the specific orbital angular momentum is 0.048. Systems with low specific orbital angular momentum values have been suspected to result from collisions (e.g., Canup 2005; Descamps and Marchis 2008) although gravitational collapse could also make binary systems with orbital angular momenta in this range (e.g., Nesvorný et al. 2010).

If we assume G!kún‖'hòmdímà has a uniform internal mass distribution and its spin period is between 11 and 41 hours, then its specific spin angular momentum would be between 0.12 and 0.03, comparable to or larger than the specific orbital angular momentum of 0.048. Exchanging angular momentum between G!ò'é !hú's orbit and G!kún‖'hòmdímà's spin has the potential to significantly alter both of them. Such a thing could have happened if the system formed through

fission of a rapidly spinning body, with tidal interaction transferring spin angular momentum into a gradually widening mutual orbit.

Another mechanism that could trigger angular momentum exchange between the mutual orbit and the spins of the component bodies involves the Kozai-Lidov mechanism whereby the solar gravitational perturbation excites cycles of high orbital eccentricity (e.g., Kozai 1962; Lidov 1962). At times in these cycles when the eccentricity is high, tidal dissipation of orbital energy in the interiors of the bodies can transfer angular momentum from their mutual orbit to the spins of the bodies (e.g., Naoz et al. 2010; Fang and Margot 2012; Porter and Grundy 2012). This effect requires a high inclination between the heliocentric orbit plane and the binary's mutual orbit plane. Systems like Orcus-Vanth and Varda-Ilmarë do indeed have high inclinations, but the mutual orbit of G!kúnǁ'hòmdímà and G!ò'é !hú is only inclined to its heliocentric orbit by 32°, so Kozai-Lidov cycles seem unlikely to have played much of a role in modifying the mutual orbit. Furthermore, perturbations from the non-spherical shape of G!kúnǁ'hòmdímà dominate over perturbations from solar tides for orbital separations less than a_{crit}, computed as

$$a_{\text{crit}} = \left(2 J_2 \frac{M_{\text{sys}}}{M_\odot} R_1^2 a_\odot^3 \right)^{\frac{1}{5}} , \qquad \text{(Eq. 6)}$$

where J_2 is the 2nd moment of G!kúnǁ'hòmdímà's gravity field, corresponding to its oblateness (Nicholson et al. 2008). For a_{crit} to be as small as 6035 km so that solar tides could compete in this system, the J_2 of G!kúnǁ'hòmdímà would have to be less than 5×10^{-7}. That is an absurdly low value, considering the elliptical limb profile revealed by the 2014 stellar occultation. Finally, the ~10^{10} year timescale for significant tidal interaction also indicates that this mechanism is unlikely to have played a role in the evolution of G!ò'é !hú's orbit.

Mutual events

During 2018, we viewed the mutual orbit of G!kúnǁ'hòmdímà and G!ò'é !hú from about 27° below the plane of the orbit. If the orbit pole and the spin pole of G!kúnǁ'hòmdímà coincide, the subsolar latitude would be −27°. This angle is changing as G!kúnǁ'hòmdímà approaches its perihelion in 2046. Soon after perihelion, in late 2050, the plane of the mutual orbit will sweep across the Sun, ignoring the possibility that the satellite's orbit precesses. If the spin and orbit poles are aligned, equinox would occur at the same time, with the subsolar latitude crossing the equator into the northern hemisphere. This occurrence also provides an opportunity to observe mutual events. Since the orbital period of G!ò'é !hú is relatively short, there will be numerous events: two every 11.3 days over the course of a mutual event season that will last for most of a decade. The fact that the mutual event season approximately coincides with perihelion means that the system will be relatively bright at a *V* magnitude of about 19, and at a moderate declination (about +16°), making it accessible to moderate-sized telescopes in both hemispheres. During the Pluto-Charon mutual events, which also happened to coincide with perihelion, only the Charon-facing hemisphere of Pluto could be mapped using mutual events, due to the two bodies having tidally locked spins. But with G!kúnǁ'hòmdímà and G!ò'é !hú, the more rapid

rotation of G!kún‖'hòmdímà could potentially allow all longitudes to be probed by mutual events. Although it seems suspicious, the alignment of perihelion and equinox for both systems during the present epoch is just a coincidence. The mutual and heliocentric orbits evolve in different ways over different timescales (e.g., Dobrovolskis et al. 1997; Earle and Binzel 2015).

Discussion

We have determined the mutual orbit of G!kún‖'hòmdímà and its satellite G!ò'é !hú from high spatial resolution images of the system obtained between 2008 and 2018. The orbit is prograde and nearly circular, with a relatively low inclination between it and the system's heliocentric orbit, and possibly also between it and G!kún‖'hòmdímà's equator, as indicated by the limb profile from the 2014 stellar occultation. The orbit is wide enough that tidal evolution probably has not much affected the system over the age of the solar system, apart from possibly locking the spin of G!ò'é !hú to its orbital period. Without substantial subsequent tidal modification, a near-circular orbit is unlikely to occur through any type of capture mechanism. The circular, and possibly aligned orbit of G!ò'é !hú suggests that the system could have formed through some sort of fission process or else it could have collapsed into something much like its present state directly from the nebula, with an excess of angular momentum causing the formation of a binary pair instead of a single object (e.g., Nesvorný et al. 2010; Simon et al. 2016, 2017). Grundy et al. (2019) present an analysis of the distribution of orbital orientations of transneptunian binaries, finding that the majority of them are prograde, as is true of the mutual orbit of G!kún‖'hòmdímà and G!ò'é !hú. They argue that this pattern favors gravitational collapse over capture or oblique impact binary-formation scenarios. The excess of angular momentum in such systems could be expected to result in similarly oriented spins and mutual orbits.

The orbit enables us to compute the system mass, which we divide by the volume estimated from thermal observations and a stellar occultation to compute a low bulk density of 1.04 ± 0.17 g cm^{-3}. With this low density but a diameter of around 630 km, G!kún‖'hòmdímà occupies an especially interesting size and density range. Densities measured for smaller TNOs tend to be low, less than 1 g cm^{-3}. Densities of larger, planet-sized TNOs are higher, around 2 g cm^{-3}. Brown (2013) argued that icy objects as large as the 700 km diameter 55637 should collapse their internal pore space, so the low densities of objects like 55637 and G!kún‖'hòmdímà imply bulk compositions with very little rocky material. However, the large planet-sized TNOs do contain significant rock (e.g., McKinnon et al. 2017), as do much smaller comet nuclei (e.g., Nagdimunov et al. 2014; Lamy et al. 2015; Fulle et al. 2017, 2019), presenting a puzzle as to how large, rock-rich TNOs could have been assembled from rock-poor mid-sized TNOs with diameters in the 400 to 1000 km range. Or, if they were assembled from smaller, rocky planetesimals, it is equally puzzling that rocky mid-sized TNOs would not also have been produced.

We suggest that the mid-sized TNOs could in fact be rock-rich, too, but some of them have low densities because they still retain substantial internal pore space. This hypothesis brings

their bulk compositions into line with the rock-rich compositions of larger TNOs as well as those of much smaller comet nuclei, and it is also consistent with expectation for the compositions of objects that accreted in the outer protoplanetary nebula rather than the giant planet sub-nebulae (e.g., McKinnon et al. 1997). We regard it as an open question whether mid-sized TNOs with diameters as large as 700 km really can retain substantial internal porosity. Laboratory studies on the compaction of cold, rock-rich ice+rock mixtures at pressures in the 1 to 100 MPa range would be extremely valuable for addressing this question.

We speculate that 600 to 700 km diameter objects like G!kún‖'hòmdímà and 55637 could represent the upper limit to retain substantial internal pore space and that by the time an object reaches 900 km, most of its internal pore space has been lost. An object that grows to 900 km diameter with a bulk density of 0.6 g cm^{-3} (corresponding to 75% pore space for a rock-rich composition) only reaches a pressure of 10 MPa at its core. If such an object formed cold and too late to incorporate appreciable ^{26}Al or ^{60}Fe, this pressure would be insufficient to collapse much pore space. But eventually, heating from long-lived radionuclides would begin to warm the interior, at which point pore space in the center would begin to collapse, causing the object to shrink. Some bodies now in this size range apparently went on to differentiate, though if they went through a cold, low density phase first, they would have been even larger before collapsing their pore space. Orcus and Charon probably melted and differentiated, considering their higher densities and spectra indicating surfaces made of relatively clean H_2O ice. But the lower albedos and densities of G!kún‖'hòmdímà, 55637, Varda, and Salacia suggest that they never did differentiate, or if they did, it was only in their deep interiors, not a complete melting and overturning that involved the surface. Their surfaces could remain quite cold and uncompressed even as the interior becomes warm and collapses. The liberation of volatiles could further help transport heat out of their interiors, limiting the extent of their internal collapse. An object with a cold, relatively pristine surface and a partially-collapsed interior should exhibit very distinctive surface geology, with abundant thrust faults indicative of the reduction in total surface area as the interior compresses and shrinks.

Different nebular solid compositions are certainly plausible, with "snow-lines" for different volatile materials occurring in various places. But even if their bulk compositions were all identical, a variety of factors could influence how much internal compaction different mid-sized TNOs experienced, leading to a diversity in bulk densities. In addition to size and the rate of formation (and thus incorporation of short-lived radionuclides), we should consider other factors. For instance, the role of impacts could be important in depositing heat and also in compressing porous material. Objects that formed through direct gravitational collapse from over-dense regions of the nebula might not get much compression from impacts, whereas objects that formed through subsequent higher speed collisions between low-density progenitor objects could be much more compacted. It would be useful to get the densities of a larger sample of mid-sized TNOs to see how diverse they are. Ideally, we would compare objects with similar sizes, colors, and dynamical settings that might be expected to have formed in similar nebular regions.

Acknowledgments

This work is based in part on NASA/ESA Hubble Space Telescope programs 11113 and 15233. Support for these programs was provided by the National Aeronautics and Space Administration (NASA) through grants from the Space Telescope Science Institute (STScI), operated by the Association of Universities for Research in Astronomy, Inc., (AURA) under NASA contract NAS 5-26555. We thank L. Dressel and B. Porterfield for their expertise and help optimizing the design and scheduling of the observations.

Additional data were obtained at the W.M. Keck Observatory, which is operated as a scientific partnership among the California Institute of Technology, the University of California, and NASA and made possible by the generous financial support of the W.M. Keck Foundation. These data were obtained from telescope time allocated to NASA through the agency's scientific partnership with the California Institute of Technology and the University of California. Acquisition of the data was supported by NASA Keck PI Data Awards, administered by the NASA Exoplanet Science Institute. We thank A. Conrad, H. Tran, C. Jordan, and H. Hershey for their expertise and help with the telescope and instrument. We recognize and acknowledge the significant cultural role and reverence of the summit of Mauna Kea within the indigenous Hawaiian community. We are most fortunate to have the opportunity to conduct observations from this mountain.

We are grateful to two anonymous reviewers for constructive suggestions and encouragement, and we thank the free and open source software communities for empowering us with key tools used to complete this project, notably Linux, the GNU tools, LibreOffice, MySQL, Evolution, Python, the Astronomy Users Library, and FVWM.

References

Baer, J., S.R. Chesley, and R.D. Matson 2011. Astrometric masses of 26 asteroids and observations on asteroid porosity. *Astron. J.* **141,** 143.1-12.

Barr, A.C., and M.E. Schwamb 2016. Interpreting the densities of the Kuiper belt's dwarf planets. *Mon. Not. R. Astron. Soc.* **460,** 1542-1548.

Bellini, A., J. Anderson, and L.R. Bedin 2011. Astrometry and photometry with HST WFC3 II: Improved geometric-distortion corrections for 10 filters of the UVIS channel. *Publ. Astron. Soc. Pacific* **123,** 622-637.

Benecchi, S.D., K.S. Noll, W.M. Grundy, M.W. Buie, D.C. Stephens, and H.F. Levison 2009. The correlated colors of transneptunian binaries. *Icarus* **200,** 292-303.

Benecchi, S.D., K.S. Noll, W.M. Grundy, and H.F. Levison 2010. (47171) 1999 TC_{36}, a trans-neptunian triple. *Icarus* **207,** 978-991.

Benedetti-Rossi, G., et al. (28 co-authors) 2016. Results from the 2014 November 15th multi-chord stellar occultation by the TNO (229762) 2007 UK_{126}. *Astron. J.* **152,** 156.1-11.

Biesele, M. 1993. *Women Like Meat: The Folklore and Foraging Ideology of the Kalahari Ju|'hoan*. Indiana University Press, Bloomington.

Biesele, M. 2009. *Ju|'hoan Folktales: Transcriptions and English Translations: A Literacy*

Primer by and for Youth and Adults of the Ju|'hoan Community. Trafford Publishing, First Voices Programme, Victoria, B.C..

Brown, M.E. 2013. The density of mid-sized Kuiper belt object 2002 UX_{25} and the formation of the dwarf planets. *Astrophys. J. Lett.* **778,** L34.1-5.

Brown, M.E., and B.J. Butler 2017. The density of mid-sized Kuiper belt objects from ALMA thermal observations. *Astron. J.* **154,** 19.1-7.

Brown, M.E., et al. (14 co-authors) 2006. Satellites of the largest Kuiper belt objects. *Astrophys. J.* **639,** L43-L46.

Brown, M.E., D. Ragozzine, J. Stansberry, and W.C. Fraser 2010. The size, density, and formation of the Orcus-Vanth system in the Kuiper belt. *Astron. J.* **139,** 2700-2705.

Canup, R.M. 2005. A giant impact origin of Pluto-Charon. *Science* **307,** 546-550.

Carry, B., et al. (10 co-authors) 2011. Integral-field spectroscopy of (90482) Orcus-Vanth. *Astron. & Astrophys.* **534,** A115.1-9.

Descamps, P., and F. Marchis 2008. Angular momentum of binary asteroids: Implications for their possible origin. *Icarus* **193,** 74-84.

Dickens, P.J. 1994. *English-Ju|'hoan, Ju|'hoan-English dictionary*. Rüdiger Köppe Verlag, Quellen zur Khoisan-Forschung 8, Köln.

Dobrovolskis, A.R., S.J. Peale, and A.W. Harris 1997. Dynamics of the Pluto-Charon binary. In: S.A. Stern, D.J. Tholen (Eds.), *Pluto and Charon*, University of Arizona Press, Tucson, 159-190.

Dolphin, A.E. 2009. A revised characterization of the WFPC2 CTE loss. *Publ. Astron. Soc. Pacific* **121,** 655-667.

Dressel, L. 2018. Wide Field Camera 3 instrument handbook. Version 10 (STScI, Baltimore, available at http://www.stsci.edu/hst/wfc3/documents/handbooks/currentIHB/wfc3_cover.html).

Durham, W.B., W.B. McKinnon, and L.A. Stern 2005. Cold compaction of water ice. *Geophys. Res. Lett.* **32,** L18202.1-5.

Earle, A.M., and R.P. Binzel 2015. Pluto's insolation history: Latitudinal variations and effects on atmospheric pressure. *Icarus* **250,** 405-412.

Elliot, J.L., et al. (10 co-authors) 2005. The Deep Ecliptic Survey: A search for Kuiper belt objects and Centaurs. II. Dynamical classification, the Kuiper belt plane, and the core population. *Astron. J.* **129,** 1117-1162 (see http://www.boulder.swri.edu/~buie/kbo/desclass.html for current Deep Ecliptic Survey team classifications).

Fang, J., and J.L. Margot 2012. The role of Kozai cycles in near-Earth binary asteroids. *Astron. J.* **143,** 59.1-8.

Fornasier, S., et al. (19 co-authors) 2013. TNOs are Cool: A survey of the transneptunian region VIII. Combined Herschel PACS and SPIRE observations of nine bright targets at 70-500 μm. *Astron. & Astrophys.* **555,** A15.1-22.

Fulle, M, V. Della Corte, A. Rotundi, S.F. Green, M. Accolla, L. Colangeli, M. Ferrari, S. Ivanovski, R. Sordini, and V. Zakharov 2017. The dust-to-ices ratio in comets and Kuiper belt objects. *Mon. Not. R. Astron. Soc.* **469,** S45-S49.

Fulle, M., J. Blum, S.F. Green, B. Gundlach, A. Herique, F. Moreno, S. Mottola, A. Rotundi, and C. Snodgrass 2019. The refractory-to-ice mass ratio in comets. *Mon. Not. R. Astron. Soc.* **482,** 3326-3340.

Giauque, W.F., and J.W. Stout 1936. The entropy of water and the third law of thermodynamics: The heat capacity of ice from 15 to 273K. *J. Am. Chem. Soc.* **58,** 1144-1150.

Gladman, B., D.D. Quinn, P. Nicholson, and R. Rand 1996. Synchronous locking of tidally evolving satellites. *Icarus* **122,** 166-192.

Gladman, B., B.G. Marsden, and C. VanLaerhoven 2008. Nomenclature in the outer Solar System. In: A. Barucci, H. Boehnhardt, D. Cruikshank, A. Morbidelli (Eds.), *The Solar System Beyond Neptune*, University of Arizona Press, Tucson, 43-57.

Goldreich, P., and S. Soter 1966. Q in the solar system. *Icarus* **5,** 375-389.

Grundy, W.M., K.S. Noll, J. Virtanen, K. Muinonen, S.D. Kern, D.C. Stephens, J.A. Stansberry, H.F. Levison, and J.R. Spencer 2008. (42355) Typhon-Echidna: Scheduling observations for binary orbit determination. *Icarus* **197,** 260-268.

Grundy, W.M., K.S. Noll, M.W. Buie, S.D. Benecchi, D.C. Stephens, and H.F. Levison 2009. Mutual orbits and masses of six transneptunian binaries. *Icarus* **200,** 627-635.

Grundy, W.M., K.S. Noll, F. Nimmo, H.G. Roe, M.W. Buie, S.B. Porter, S.D. Benecchi, D.C. Stephens, H.F. Levison, and J.A. Stansberry 2011. Five new and three improved mutual orbits of transneptunian binaries. *Icarus* **213,** 678-692.

Grundy, W.M., et al. (11 co-authors) 2012. Mutual events in the cold classical transneptunian binary system Sila and Nunam. *Icarus* **220,** 74-83.

Grundy, W.M., S.D. Benecchi, S.B. Porter, and K.S. Noll 2014. The orbit of transneptunian binary Manwë and Thorondor and their upcoming mutual events. *Icarus* **237,** 1-8.

Grundy, W.M., S.B. Porter, S.D. Benecchi, H.G. Roe, K.S. Noll, C.A. Trujillo, A. Thirouin, J.A. Stansberry, E. Barker, and H.F. Levison 2015. The mutual orbit, mass, and density of the large transneptunian binary system Varda and Ilmarë. *Icarus* **257,** 130-138.

Grundy, W.M., et al. (10 co-authors) 2019. Mutual orbit orientations of transneptunian binaries. *Icarus* (this volume).

Hainaut, O.R., and A.C. Delsanti 2002. Colors of minor bodies in the outer solar system: A statistical analysis. *Astron. & Astrophys.* **389,** 641-664.

Hastings, D.M., D. Ragozzine, D.C. Fabrycky, L.D. Burkhart, C. Fuentes, J.L. Margot, M.E. Brown, and M. Holman 2016. The short rotation period of Hi'iaka, Haumea's largest satellite. *Astron. J.* **152,** 195.1-12.

Hubbard, W.B. 1984. *Planetary interiors*. Van Nostrand Reinhold Co., New York.

Jorda, L., et al. (47 co-authors) 2016. The global shape, density and rotation of Comet 67P/Churyumov-Gerasimenko from preperihelion Rosetta/OSIRIS observations. *Icarus* **277,** 257-278.

Kiss, C., G. Marton, A. Farkas-Takacs, J. Stansberry, T. Muller, J. Vinko, Z. Balog, J.L. Ortiz, and A. Pal 2017. Discovery of a satellite of the large trans-neptunian object (225088) 2007 OR_{10}. *Astrophys. J. Lett.* **838,** L1.1-5.

Kozai, Y. 1962. Secular perturbations of asteroids with high inclination and eccentricity. *Astron.*

J. **67,** 591-598.

Krist, J.E., R.N. Hook, and F. Stoehr 2011. 20 years of Hubble Space Telescope optical modeling using Tiny Tim. *Proc. SPIE* **8127,** 1-16.

Lamy, P.L., A. Herique, and I. Toth 2015. The subsurface structure and density of cometary nuclei. *Space Sci. Rev.* **197,** 85-99.

Le Mignant, D., et al. (18 co-authors) 2006. LGS AO at W.M. Keck Observatory: Routine operations and remaining challenges. *Proc. SPIE* **6272,** 627201.

Lidov, M.L. 1962. The evolution of orbits of artificial satellites of planets under the action of gravitational perturbations of external bodies. *Planet. Space. Sci.* **9,** 719-759.

McKinnon, W.B., D.P. Simonelli, and G. Schubert 1997. Composition, internal structure, and thermal evolution of Pluto and Charon. In: S.A. Stern, D.J. Tholen (Eds.), *Pluto and Charon*, University of Arizona Press, Tucson, 295-343.

McKinnon, W.B., D. Prialnik, S.A. Stern, and A. Coradini 2008. Structure and evolution of Kuiper belt objects and dwarf planets. In: A. Barucci, H. Boehnhardt, D. Cruikshank, A. Morbidelli (Eds.), *The Solar System Beyond Neptune*, University of Arizona Press, Tucson, 213-241.

McKinnon, W.B., et al. (13 co-authors) 2017. Origin of the Pluto-Charon system: Constraints from the New Horizons flyby. *Icarus* **287,** 2-11.

McMaster, M., et al. (39 co-authors) 2008. *WFPC2 instrument handbook*, Version 10.0. Space Telescope Science Institute, Baltimore, available at http://www.stsci.edu/hst/wfpc2.

Merk, R., and D. Prialnik 2003. Early thermal and structural evolution of small bodies in the transneptunian zone. *Earth, Moon, & Planets* **92,** 359-374.

Merk, R., and D. Prialnik 2006. Combined modeling of thermal evolution and accretion of trans-neptunian objects: Occurrence of high temperatures and liquid water. *Icarus* **183,** 283-295.

Mohr, P.J., B.N. Taylor, and D.B. Newell 2008. CODATA recommended values of the fundamental physical constants: 2006. *Rev. Mod. Phys.* **80,** 633-730.

Murray, C.D., and S.F. Dermott 1999. *Solar system dynamics*. Cambridge University Press, New York.

Nagdimunov, L., L. Kolokolova, M. Wolff, M.F. A'Hearn, and T.L. Farnham 2014. Properties of comet 9P/Tempel 1 dust immediately following excavation by deep impact. *Planet. Space Sci.* **100,** 73-78.

Naoz, S., H.B. Perets, and D. Ragozzine 2010. The observed orbital properties of binary minor planets. *Astrophys. J.* **719,** 1775-1783.

Nelder, J., and R. Mead 1965. A simplex method for function minimization. *Computer Journal* **7,** 308-313.

Nesvorný, D., A.N. Youdin, and D.C. Richardson 2010. Formation of Kuiper belt binaries by gravitational collapse. *Astron. J.* **140,** 785-793.

Nicholson, P.D., M. Cuk, S.S. Sheppard, D. Nesvorný, and T.V. Johnson 2008. Irregular satellites of the giant planets. In: A. Barucci, H. Boehnhardt, D. Cruikshank, A. Morbidelli (Eds.), *The Solar System Beyond Neptune*, University of Arizona Press, Tucson, 411-424.

Noll, K.S., W.M. Grundy, E.I. Chiang, J.L. Margot, and S.D. Kern 2008. Binaries in the Kuiper

belt. In: A. Barucci, H. Boehnhardt, D. Cruikshank, A. Morbidelli (Eds.), *The Solar System Beyond Neptune*, University of Arizona Press, Tucson, 345-363.

Noll, K.S., W.M. Grundy, S.D. Benecchi, H.F. Levison, and E.A. Barker 2009. Discovery of eighteen transneptunian binaries. *Bull. Amer. Astron. Soc.* **41,** 1092 (abstract).

Omura, T., and A.M. Nakamura 2018. Estimating the porosity structure of granular bodies using the Lane-Emden equation applied to laboratory measurements of the pressure-density relation of fluffy granular samples. *Astrophys. J.* **860,** 123.1-7.

Ortiz, J.L., et al. (92 co-authors) 2017. The size, shape, density and ring of the dwarf planet Haumea from a stellar occultation. *Nature* **550,** 219-223.

Parker, A.H., M.W. Buie, W.M. Grundy, and K.S. Noll 2016. Discovery of a Makemakean moon. *Astrophys. J. Lett.* **825,** L9.1-5.

Perna, D., M.A. Barucci, S. Fornasier, F.E. DeMeo, A. Alvarez-Candal, F. Merlin, E. Dotto, A. Doressoundiram, and C. de Bergh 2010. Colors and taxonomy of Centaurs and trans-Neptunian objects. *Astron. & Astrophys.* **510,** A53.1-7.

Porter, S.B., and W.M. Grundy 2012. KCTF evolution of transneptunian binaries: Connecting formation to observation. *Icarus* **220,** 947-957.

Press, W.H., S.A. Teukolsky, W.T. Vetterling, and B.P. Flannery 1992. *Numerical Recipes in C*. Cambridge University Press, New York.

Prialnik, D., G. Sarid, E.D. Rosenberg, and R. Merk 2008. Thermal and chemical evolution of comet nuclei and Kuiper belt objects. *Space Sci. Rev.* **138,** 147-164.

Ryan, E.L., B.N.L. Sharkey, and C.E. Woodward 2017. Trojan asteroids in the Kepler Campaign 6 field. Astron. J. 153, 116.1-12.

Santos-Sanz, P., et al. (22 co-authors) 2012. "TNOs are Cool": A survey of the transneptunian region. IV. Size/albedo characterization of 15 scattered disk and detached objects observed with Herschel-PACS. *Astron. & Astrophys.* **541,** A92.1-18.

Schindler, K., et al. (10 co-authors) 2017. Results from a triple chord stellar occultation and far-infrared photometry of the transneptunian object (229762) 2007 UK_{126}. *Astron. & Astrophys.* **600,** A12.1-16.

Schwamb, M.E, M.E. Brown, D. Rabinowitz, and B.G. Marsden 2008. 2007 UK126. *Minor Planet Electronic Circ.*, No. 2008-D38.

Schwamb, M.E., M.E. Brown, and D.L. Rabinowitz 2009. A search for distant Solar System bodies in the region of Sedna. *Astrophys. J.* **694,** L45-L48.

Schwamb, M.E., M.E. Brown, D.L. Rabinowitz, and D. Ragozzine 2010. Properties of the distant Kuiper belt: Results from the Palomar Distant Solar System Survey. *Astrophys. J.* **720,** 1691-1707.

Sicardy, B., et al. (72 co-authors) 2011. A Pluto-like radius and a high albedo for the dwarf planet Eris from an occultation. *Nature* **478,** 493-496.

Simon, J.B., P.J. Armitage, R. Li, and A.N. Youdin 2016. The mass and size distribution of planetesimals formed by the streaming instability. I: The role of self-gravity. *Astrophys. J.* **822,** 55.1-18.

Simon, J.B., P.J. Armitage, A.N. Youdin, and R. Li 2017. Evidence for universality in the initial

planetesimal mass function. *Astrophys. J. Lett.* **847,** L12.1-6.
Stansberry, J.A., W.M. Grundy, M. Mueller, S.D. Benecchi, G.H. Rieke, K.S. Noll, M.W. Buie, H.F. Levison, S.B. Porter, and H.G. Roe 2012. Physical properties of transneptunian binaries (120347) Salacia-Actaea and (42355) Typhon-Echidna. *Icarus* **219,** 676-688.
Thirouin, A., K.S. Noll, J.L. Ortiz, and N. Morales 2014. Rotational properties of the binary and non-binary populations in the transneptunian belt. *Astron. & Astrophys.* **569,** A3.1-20.
Vilenius, E., et al. (22 co-authors) 2012. "TNOs are Cool": A survey of the trans-neptunian region. VI. Herschel/PACS observations and thermal modeling of 19 classical Kuiper belt objects. *Astron. & Astrophys.* **541,** A94.1-17.
Vilenius, E., et al. (16 co-authors) 2014. "TNOs are Cool": A survey of the trans-neptunian region X. Analysis of classical Kuiper belt objects from Herschel and Spitzer observations. *Astron. & Astrophys.* **564,** A35.1-18.
Yoder, C.F. 1982. Tidal rigidity of Phobos. *Icarus* **49,** 327-346.
Youdin, A.N., and J. Goodman 2005. Streaming instabilities in protoplanetary disks. *Astrophys. J.* **620,** 459-469.

2008-11-13	6.64528	45.566	44.65817	0.50	-0.08708	0.00371	-0.12151	0.00280	3.658	0.166
2009-12-11	8.19085	45.179	44.33387	0.65	-0.13552	0.00600	-0.00385	0.00600	3.088	0.090
2009-12-12	7.86932	45.178	44.33901	0.66	-0.18020	0.00600	-0.06806	0.00600	3.117	0.100
2018-01-02	14.81575	42.450	41.67363	0.82	-0.13566	0.00354	-0.13399	0.00139	3.168	0.085
2018-01-03	11.25583	42.449	41.68046	0.83	-0.08324	0.00394	-0.13567	0.00100	3.297	0.077
2018-03-27	7.60542	42.378	42.79690	1.22	+0.16284	0.00260	+0.08656	0.00100	3.389	0.048
2018-03-31	6.74712	42.375	42.84963	1.18	-0.05961	0.06000	-0.00461	0.06000	-	
2018-08-04	23.05375	42.267	42.73237	1.22	-0.16166	0.00100	-0.10611	0.00151	3.212	0.026

2018-01-02	19.5278	0.0231	19.7608	0.0231	18.6458	0.0296	18.6530	0.0297
23.0338	0.0769	23.4920	0.0771	21.7545	0.0923	21.7957	0.0925	
2018-01-03	19.6603	0.0581	19.8933	0.0581	18.9538	0.0315	18.9608	0.0315
23.3271	0.0337	23.7851	0.0337	21.6538	0.1592	21.6948	0.1592	
2018-03-27	19.6085	0.0085	19.8415	0.0085	18.8167	0.0222	18.8237	0.0222
23.3244	0.0631	23.7829	0.0632	21.8851	0.0974	21.9261	0.0974	
2018-08-04	19.6070	0.0185	19.8400	0.0185	18.8363	0.0412	18.8433	0.0412
23.1259	0.1239	23.5839	0.1239	21.8667	0.0431	21.9077	0.0432	